Chinese Chemical Letters 37 (2026) 112787

Contents lists available at ScienceDirect

Chinese Chemical Letters

journal homepage: www.elsevier.com/locate/cclet

Dual-guest co–intercalation engineering enables high-energy and long-life aqueous zinc-ion batteries

Chengjun Wu[a], Yajiang Wang[a], Xiaoduo Jiang[a], Huixiong Jiang[a], Jin-Hang Liu[a], Ping Yan[a], Hai-Yan Hu[b], Yao Xiao[b,*], Xiudong Chen[a,*]

[a] School of Chemistry and Chemical Engineering, Jiangxi Province Engineering Research Center of Ecological Chemical Industry, Jiujiang University, Jiujiang 332005, China
[b] College of Chemistry and Materials Engineering, Wenzhou University, Wenzhou 325035, China

ARTICLE INFO

Article history:
Received 4 February 2026
Revised 27 March 2026
Accepted 16 April 2026
Available online 16 April 2026

Keywords:
Dual-guest co-intercalation
Ammonium vanadate
Electronic structure modulation
Aqueous zinc-ion batteries
Ion diffusion kinetics

ABSTRACT

Ammonium vanadate (NVO) is an attractive cathode material for aqueous zinc-ion batteries (AZIBs) owing to its tunable layered structure. However, its practical use is limited by structural instability and irreversible NH_4^+ extraction during cycling. To overcome these challenges, we employed a dual-guest pillar strategy for NVO, utilising a one-pot hydrothermal co-intercalation technique to insert Al^{3+} and benzyltrimethylammonium ions ($BTMA^+$) into its interlayer spacing. The synergistic intercalation of Al^{3+} and $BTMA^+$ not only expanded the interlayer spacing to 10.9 Å but also further modulated the electronic structure. Simulations reveal a narrowed band gap and enhanced Zn^{2+} adsorption capability, which synergistically boost rapid Zn^{2+} migration and enhance structural stability. Consequently, the resultant cathode delivers a high specific capacity of 432.8 mAh/g at 1.0 A/g, alongside excellent rate capability and cycling stability (92.07 % capacity retention after 2000 cycles at 6.0 A/g). This work demonstrates that dual-guest co-intercalation-enabled molecular pillaring and electronic modulation is an effective strategy for fabricating high-performance vanadium-based cathodes for advanced AZIBs.

© 2026 Published by Elsevier B.V. on behalf of Chinese Chemical Society and Institute of Materia Medica, Chinese Academy of Medical Sciences.

With the rapid advancement of technology and industry globally, the need for urgent solutions to address the dual challenges of escalating energy demand and worsening environmental pollution has never been more urgent. Hence, the replacement of fossil fuels (*e.g.*, petroleum and coal) necessitates the development and utilization of renewable and clean energy sources, such as solar, wind, and geothermal power. Although these renewable energy sources are readily available, their intermittentity and storage instability restrict their application to grid-scale energy storage systems [1–3]. Given their portability, batteries are of significant research interest owing to their portability. Years of intensive research and development have led to significant improvements in the energy and power density of lithium-ion batteries (LIBs), positioning them as the predominant energy storage devices in use today. LIBs, however, are subject to several significant constraints. Globally limited lithium resources, coupled with rising future market demand, lead to high costs. Nevertheless, their widespread application is constrained by the inherent limitations of toxic organic electrolytes and extremely reactive lithium [4,5]. Due to the exceptional safety and environmental friendliness of aqueous batteries, they are considered to be an ideal choice for storing large quantities of energy on a large scale. Among them, aqueous zinc-ion batteries (AZIBs) are a highly promising energy storage technology, boasting a high theoretical capacity (820 mAh/g) and a low redox potential (−0.76 V *vs.* SHE), positioning them as a formidable candidate for abundant resources, high energy density, inherent safety, and environmental sustainability [6–8].

There are still challenges facing the current generation of AZIBs, such as a low energy density and short cycling life. To address these issues, researchers are developing high-performance cathode materials, including analogs of Prussian blue, manganese-based materials, organic compounds, and vanadium-based materials. These materials exhibit diverse electrochemical behaviors depending on how they are synthesized, their chemical compositions, and their crystal structures. Due to their high theoretical capacities and multiple valence states, vanadium-based materials have played a pivotal role in the advancement of AZIBs [9–12]. Owing to the large interlayer spacing of NVO (9.8 Å), more active sites can be exposed and the space is available for the intercalation and deintercalation of Zn^{2+} thus enabling fast ion transport. Nevertheless, NVO has the potential to undergo structural degradation during

* Corresponding authors.
E-mail addresses: xiaoyao@wzu.edu.cn (Y. Xiao), chenxd@jju.edu.cn (X. Chen).

https://doi.org/10.1016/j.cclet.2026.112787
1001-8417/© 2026 Published by Elsevier B.V. on behalf of Chinese Chemical Society and Institute of Materia Medica, Chinese Academy of Medical Sciences.

prolonged cycling, resulting in the collapse of the framework and irreversible deammoniation, which inhibits its use in AZIBs. Different strategies have been employed to overcome these limitations, including the intercalation of guest species (*e.g.*, water molecules, organic molecules, anions, cations), defect engineering, and modification of heterointerfaces. To effectively expand the interlayer spacing, metal cations (*e.g.*, Na^+, K^+, NH_4^+, Ni^{2+}, Rb^+) can be pre-intercalated, leading to enhanced specific capacity and superior cycling stability [13–15]. There are still limitations to single-metal-ion intercalation, such as its ineffectiveness and the risk of ion detachment, as well as its inability to address the problem of narrow ion transport channels. Studies have indicated that organic molecules with flexible frameworks (*e.g.*, aniline, poly(3,4-ethylenedioxythiophene), ethylene glycol, and ethylenediamine) can effectively shield the electrostatic interaction between Zn^{2+} ions and V-O bonds, stabilizing the NVO structure, improving electrochemical stability, and allowing Zn^{2+} to be stored efficiently. Organic intercalation agents, owing to their insufficient electrochemical stability, are prone to oxidative decomposition or dissolution in electrolytes. Single-ion intercalation strategies cannot overcome all of these challenges adequately. Therefore, a synergistic strategy of co-intercalating organic and inorganic guests into NVO interlayers has been proposed. This method not only modulates interlayer spacing and reduces electrostatic interactions but also harnesses the distinct advantages of each component.

Herein, we propose an Al^{3+}/benzyltrimethylammonium ($BTMA^+$) dual-guest co-intercalation strategy that simultaneously realizes molecular pillaring and electronic modulation of the NVO host. This synergistic modification preserves structural integrity while expanding the interlayer spacing to 10.9 Å for unobstructed Zn^{2+} migration during intercalation. Beyond structural reinforcement, $BTMA^+$ polar groups modulate the electronic structure by weakening the electrostatic attraction between Zn^{2+} and the V-O lattice, thus accelerating Zn^{2+} transport kinetics. Co-intercalation of Al^{3+} and $BTMA^+$ into NVO yields the high-performance IO–NVO cathode, whose enhanced electrochemistry stems from dual-guest-enabled pillaring and modulation synergies. Specifically, IO–NVO delivers 432.8 mAh/g at 1.0 A/g, retains 92.07 % of its initial capacity after 2000 cycles at 6.0 A/g, and achieves a 97.26 % pseudocapacitive contribution at 1.0 mV/s, indicative of fast charge storage dynamics. Systematic *ex-situ* XRD/XPS and *in-situ* Raman spectroscopy reveal that IO–NVO operates *via* H^+/Zn^{2+} co-intercalation/deintercalation; dual-guest pillaring ensures structural robustness during ion insertion/extraction, while electronic modulation optimizes transport environments, collectively underpinning IO–NVO's superior AZIB performance.

Initial $(NH_4)_2V_{10}O_{25}\cdot 8H_2O$ (NVO) was synthesized using ammonium metavanadate (NH_4VO_3) and oxalic acid dihydrate ($H_2C_2O_4\cdot 2H_2O$) as precursors. By adding benzyltrimethylammonium cations ($BTMA^+$) and Al^{3+} cations, it was possible to further modify NVO chemical properties and interlayer spacing (Fig. 1a). The I-NVO material was fabricated by intercalating Al^{3+} into the NVO interlayers. Following $BTMA^+$ incorporation into the intercalated structure, IO–NVO was formed, while O–NVO was formed with $BTMA^+$ alone. To elucidate the electronic modulation mechanism by $Al^{3+}/BTMA^+$ intercalation, DFT calculations were conducted on the NVO framework, successfully simulating the crystal structures of NVO, I-NVO, O–NVO and IO–NVO (Fig. 1b and Fig. S1 in Supporting information). The density of states (DOS) results (Figs. 1c-f) show that IO–NVO has a narrower band gap (0.33 eV) than NVO (0.94 eV), O–NVO (0.38 eV) and I-NVO (0.44 eV), which is attributed to the generation of novel electronic states within the band gap. As a dual-guest co-intercalation material with the smallest band gap, IO–NVO exhibits significantly enhanced conductivity. To further clarify the effect of structural and electronic modulation on ion transport behavior, we calculated the Zn^{2+} adsorption energy of each material system. The Zn^{2+} adsorption energy of O–NVO with only $BTMA^+$ intercalated (14.43 eV) and that of I-NVO with only Al^{3+} embedded (13.88 eV) are both higher than that of NVO (12.64 eV), while the dual-guest IO–NVO has the highest adsorption energy (14.47 eV) (Fig. 1g). This result confirms that Al^{3+} and $BTMA^+$ act as pillars between the NVO layers. The coordination of Al^{3+} between the layers stabilizes this pillar state, enhancing the binding affinity of the supporting layers for Zn^{2+} and thus improving performance. This enhanced adsorption affinity indicates that the IO–NVO structure is conducive to superior Zn^{2+} migration kinetics, thereby effectively facilitating Zn^{2+} insertion and extraction. Based on these DFT calculation results, it can be concluded that the new electronic states induced by dual-guest co-intercalation not only improve the conductivity of NVO-based materials but also optimize their ion transport performance, thus effectively improving the overall electrochemical performance of the materials.

The crystal structures of NVO, I-NVO, O–NVO, and IO–NVO were examined by X-ray diffraction (XRD). All diffraction peaks for each sample correspond well to the standard $(NH_4)_2V_{10}O_{25}\cdot 8H_2O$ (PDF #26–0097), with the pristine NVO exhibiting a characteristic (001) peak at 8.578° (Fig. 2a). The interlayer spacing was measured to be 10.1 Å. The (001) diffraction peak of IO–NVO shifts to 8.086°, confirming that the co-intercalation of Al^{3+} and $BTMA^+$ successfully expands the interlayer spacing of NVO to 10.9 Å. For comparison, the interlayer spacing of I-NVO and O–NVO increases to 10.7 Å and 10.3 Å, respectively, due to the pillaring effect of the single guest species. This result indicates that Al^{3+} exhibits a stronger pillaring effect than $BTMA^+$ in lattice expansion. In fact, the expansion of interlayer spacing depends on the strength of guest-host interactions rather than the sole size of the guest species. Specifically, Al^{3+} forms strong ionic bonds with the lattice oxygen of the V-O framework, an interaction that effectively expands the interlayer spacing to 10.7 Å. In contrast, $BTMA^+$ only interacts within the NVO interlayers *via* weak van der Waals forces. Moreover, $BTMA^+$ may displace partial interlayer water molecules, which counteracts the spacing expansion effect brought by its large radius, resulting in a relatively smaller interlayer spacing of 10.3 Å. To determine the water content, thermogravimetric analysis (TGA) was performed (Fig. 2b and Fig. S2 in Supporting information). The initial weight loss observed below 100 °C primarily corresponds to the removal of physiosorbed surface water. Subsequent weight loss stems from the elimination of bound water and NH_4^+ ions [16]. The calculated total weight losses were 9.51 % for NVO, 9.30 % for I-NVO, 10.61 % for O–NVO, and 10.18 % for IO–NVO. The difference between the samples, where IO–NVO showed a weight loss of 0.67 % attributed to $BTMA^+$ and O–NVO exhibited a weight loss of 1.51 % attributed to $BTMA^+$, stems from residual Al^{3+} and the reduction of organic $BTMA^+$ after heat treatment, whereas NH_4^+ was completely removed. This result further provided evidence for Al^{3+} and $BTMA^+$ dual-guest co-intercalation [17]. Successful intercalation was further verified by Fourier transform infrared (FTIR) spectra (Fig. 2c). The spectrum shows characteristic peaks at 498.85, 766.66, and 991.02 cm^{-1}, which are discernible and are assigned to the V-O bending vibration, V-O-V asymmetric stretching [18], and V=O stretching vibration, respectively [19]. This absorption band at 1427.33 cm^{-1} can be interpreted as N–H stretching vibration, confirming NH_4^+ presence in the sample [20]. This band can be attributed to the bending vibrations of H–O-H bonds in water molecules at 1609.66 cm^{-1} [21,22]. Characteristic peaks at 1048.63 and 1260.66 cm^{-1} in the FTIR spectrum served as direct evidence for the presence of $BTMA^+$, assigned to benzene rings and C–N groups, respectively [23,24]. To gain further structural insights, Raman spectroscopy was employed (Fig. 2d). There was a remarkable similarity in the spectra of NVO, IO–NVO, I-NVO, and O–NVO, indicating similar crystal structures. The strong peak

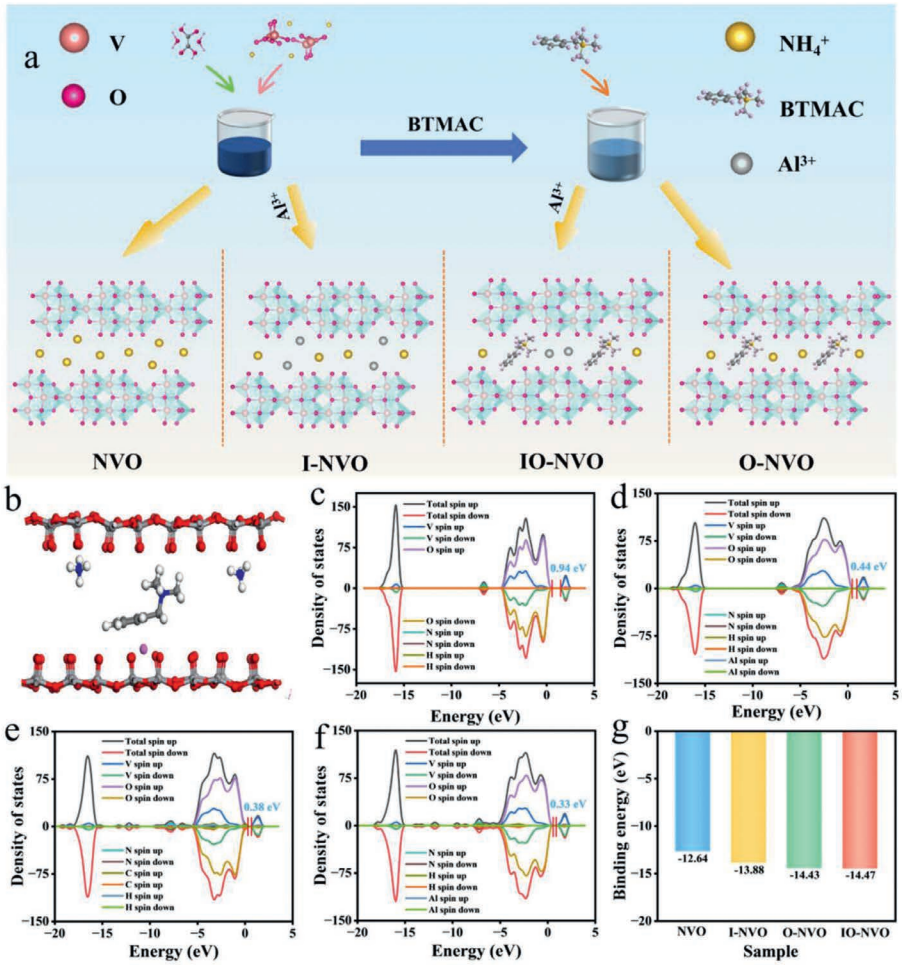


Fig. 1. Synthesis and DFT Calculations of IO–NVO, O–NVO, I-NVO, and NVO materials. (a) Schematic diagram for the preparation of IO–NVO. (b) Optimized structural geometry of IO–NVO. Illustrates the total and orbital-projected density of states (DOS) of (c) pristine NVO, (d) I-NVO, (e) O–NVO, and (f) IO–NVO. (g) Comparison of the Zn^{2+} adsorption energy on NVO, I-NVO, O–NVO, and IO–NVO.

at 147.02 cm^{-1} in the IO–NVO spectrum originates from the bending vibration of the -O-V-O- chain [25], which further supports the formation of a layered structure. The Raman vibrational bands at 266.76 and 991.71 cm^{-1} are identified as the bending modes of V=O bonds, whereas those at 406.44, 510.46, and 696.88 cm^{-1} are associated with the stretching vibrations of V-O bonds [26]. Notably, compared to the pristine NVO, the peaks at 147.02 cm^{-1}, 406.44 cm^{-1}, and 696.88 cm^{-1} all exhibit blue shifts, indicating that the increased vanadium oxidation state leads to stronger V-O interactions [27]. Furthermore, IO–NVO exhibited distinct red shifts at 266.76 and 510.46 cm^{-1}, indicating an elongation of V=O bonds along the *c*-axis and lattice expansion along the *b*-axis [28], in good agreement with XRD analysis. X-ray photoelectron spectroscopy (XPS) was used to investigate its chemical composition and valence states (Fig. S3 in Supporting information). The high-resolution Al $2p_{3/2}$ spectrum (Fig. S4 in Supporting information) shows a peak at 69.68 eV, corresponding to the Al 2p orbital, which confirms the formation of Al-O bonds [29]. In the V 2p spectrum of IO–NVO (Fig. 2e), two spin-orbit doublets ($2p_{1/2}$ and $2p_{3/2}$) were identified, with characteristic peaks located at 524.68/523.08 eV and 517.18/515.78 eV, assigned to V^{5+} and V^{4+}, respectively [30]. Absorption peaks corresponding to V-O bonds (529.88 eV) and oxygen vacancies (O_d, 530.68 eV) were observed in the O 1s spectrum (Fig. 2f). The oxygen vacancy content of each sample was calculated by the peak area ratio, showing I-NVO (1.74 %) < O–NVO (2.60 %) < IO–NVO (5.40 %), and IO–NVO has a relatively high proportion of oxygen vacancies (Fig. S5 in Supporting information), which can significantly enhance the reversible ion diffusion rate in the compound [31]. Compared with single-guest intercalation, dual-guest co-intercalation exhibits a more significant effect in introducing oxygen vacancies and improving ion diffusion. The high-resolution C 1s spectrum (Fig. 2g) displays three distinct peaks at 288.08, 285.68, and 284.61 eV, corresponding to C–O, C–N, and C–C bonds [32], respectively, confirming the successful intercalation of $BTMA^+$. This is further supported by the N 1s spectrum (Fig. 2h), in which the peaks at 401.18 eV and 399.38 eV are assigned to N–C and NH_4^+ [33], respectively, consistent with the FTIR results. Scanning electron microscopy (SEM) images of IO–NVO (Fig. S6a in Supporting information) revealed a porous structure with a needle-bundle-like morphology. Transmission electron microscopy (TEM) images (Figs. S6b and c in Supporting information) further confirmed that IO–NVO is composed of nanobelts with a lattice spacing of 10.9 Å, which corroborates the XRD findings. The structural merits of IO–NVO contribute to its higher specific capacity compared to pristine NVO. Additionally, the homogeneous co-intercalation of Al^{3+} and $BTMA^+$ within the IO–NVO structure was further verified by energy-dispersive X-ray spectroscopy (EDS) mapping (Figs. S6d-i in Supporting information), as evidenced by the uniform distribution of V, O, C, N, and Al elements. This structural advantage is further confirmed by complementary SEM characterization (Fig. S7 in Supporting information). The Brunauer-Emmett-Teller (BET) method

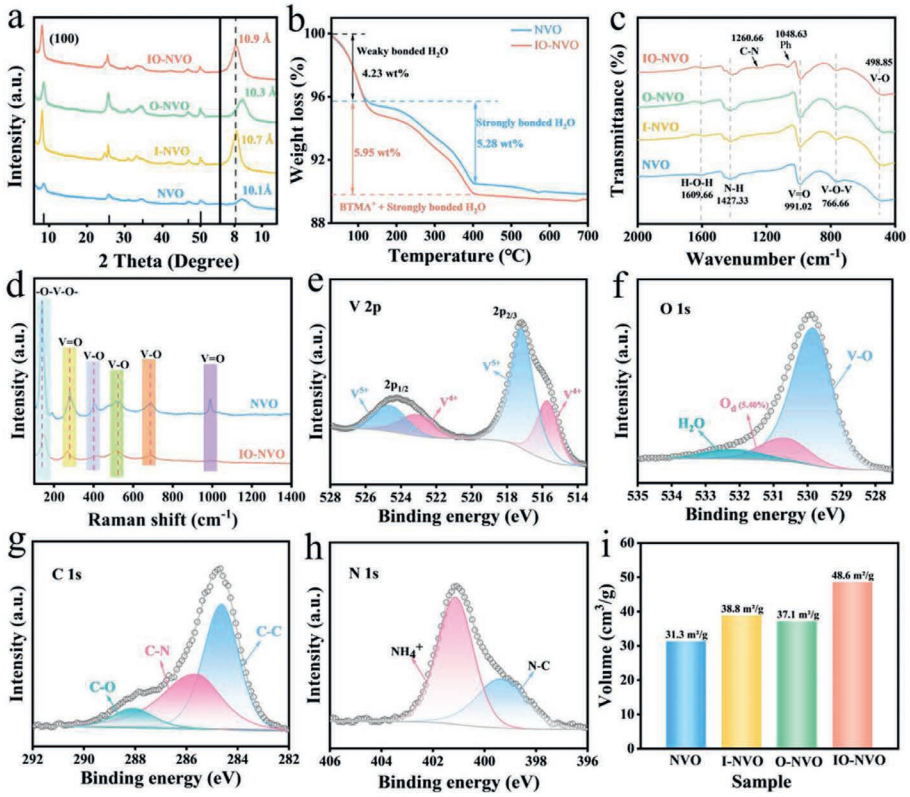


Fig. 2. Structural properties of NVO, I-NVO, O–NVO, and IO–NVO. (a) XRD patterns. (b) TGA curves. (c) FTIR spectra. (d) Raman spectra. XPS spectra of (e) V 2p, (f) O 1s, (g) N 1s, (h) C 1s. (i) Specific surface areas of NVO, I-NVO, O–NVO and IO–NVO.

was employed to investigate the structural characteristics of the samples (Fig. 2i). The dual-guest intercalated IO–NVO exhibits a specific surface area of 48.6 m^2/g, which is significantly higher than those of pristine NVO (31.3 m^2/g), I-NVO (38.8 m^2/g), and O–NVO (37.1 m^2/g) corresponding to an approximate 55.30 % increase compared with NVO. Corresponding pore structure analysis (Fig. S8 in Supporting information) confirms that IO–NVO also possesses higher porosity. In addition to providing abundant active sites for Zn^{2+} storage, the expanded specific surface area enables sufficient contact between the electrode and the electrolyte.

In coin cells with zinc foil anodes and a 2.0 mol/L $Zn(CF_3SO_3)_2$ aqueous electrolyte, electrochemical performance was assessed within a voltage window of 0.2–1.6 V. Three cyclic voltammetry (CV) cycles recorded at 0.1 mV/s (Fig. 3a) revealed three pairs of redox peaks, indicating multi-step reversible Zn^{2+} intercalation/deintercalation [34]. The V^{4+}/V^{3+} and V^{5+}/V^{4+} transitions were assigned distinct redox couples located at 0.66/0.44 V and 1.04/0.97 V, respectively. Zn^{2+} occupies interstitial sites within the polyhedra of VO when a minor redox pair is present at 1.35/1.32 V [35]. In addition to the excellent repeatability exhibited in the initial three cycles, the consistency of the galvanostatic charge discharge (GCD) curves also proves the high reversibility of the system (Fig. S9 in Supporting information), and its specific capacity performance is better than that of other electrodes. By comparing the CV curves of the four sample groups (Fig. 3a and Fig. S10 in Supporting information), it is evident that the CV curve morphology changes upon the introduction of $BTMA^+$, owing to the organic cation inducing V 3d, thereby influencing its electrochemical behavior [36]. The high-strength Al pillars serve as interlayer supports to further consolidate the layered architecture. Compared with the control samples, IO–NVO exhibits superior specific capacity and cycling stability at 1.0 A/g (Fig. 3b). The initial discharge capacity of IO–NVO (432.8 mAh/g) is higher than those of O–NVO (296.9 mAh/g), I-NVO (290.7 mAh/g) and NVO (194.7 mAh/g). It still maintains a capacity of 372.8 mAh/g (86.10 %) after 100 cycles, whose cycling performance is significantly better than that of other electrode materials. These results indicate that the synergistic effect of Al^{3+} and $BTMA^+$ can simultaneously improve the capacity and cycling stability of NVO. The IO–NVO cathode was tested within a current density range of 0.2–6.0 A/g (Fig. S11a in Supporting information), and the measured specific capacities are 424.9, 394.1, 373.4, 352.4, 323.5 and 296.8 mAh/g, respectively. When the current density is restored to 0.2 A/g, a high capacity of 388.1 mAh/g can be recovered, demonstrating excellent reversibility and rate performance. In addition, the charge-discharge curves at different current densities (Fig. S11b in Supporting information) all show two distinct platforms, which are consistent with the results of cyclic voltammetry curves. The enhanced electrochemical performance induced by dual-guest co-intercalation was further verified *via* supplementary cycling tests conducted at 0.2 A/g (Fig. S12 in Supporting information). The IO–NVO maintains a capacity of 262.1 mAh/g after 50 cycles with an initial capacity of 448.3 mAh/g. In contrast, NVO only retains a capacity of 211.5 mAh/g under the same conditions. These results suggest that Al^{3+} and $BTMA^+$ can improve the capacity and stability of NVO, and their synergistic effect is more significant. The structural stability of the material was evaluated by self-discharge test. The Zn||IO–NVO battery maintains a Coulombic efficiency (CE) of 92.90 % after standing for 48 h, which is significantly higher than that of the Zn||NVO battery (84.40 %) (Fig. 3c). After 2000 cycles at a high current density of 6.0 A/g (Fig. 3d), the IO–NVO electrode delivers a specific capacity of 320.1 mAh/g with a capacity retention rate of 92.07 %, whose performance is significantly superior to that of other samples. Compared with recently reported AZIB cathode materials, the IO–NVO electrode also exhibits superior electrochemical performance at current densities ranging from 0.2 A/g to 6.0 A/g (Fig. 3e)

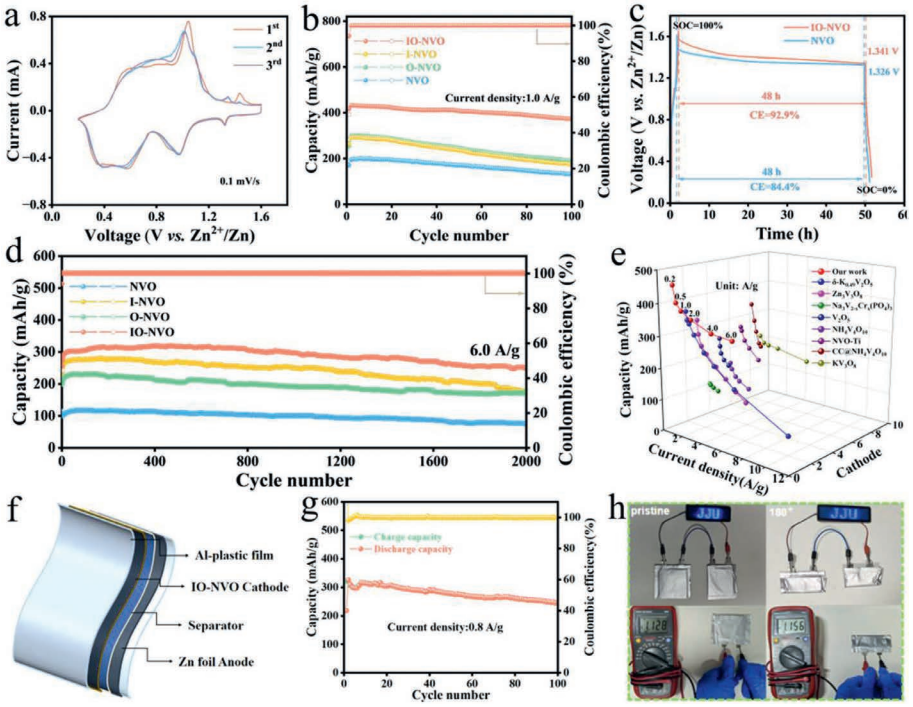


Fig. 3. Electrochemical performance of zinc-ion batteries employing NVO, I-NVO, O–NVO, and IO–NVO cathodes. (a) Cyclic voltammetry profiles at 0.1 mV/s. (b) Cycling stability of IO–NVO at 1.0 A/g. (c) Self-discharge behavior of Zn||NVO and Zn||IO–NVO configurations. (d) Long-term cycling performance of IO–NVO at 6.0 A/g. (e) Specific capacity comparison of IO–NVO with recently reported cathode materials. (f) Schematic diagram of the soft-packaged battery. (g) Cycling performance of IO–NVO soft-packaged battery at 0.8 A/g and (h) images of the LED and voltage stability powered by an IO–NVO soft-packaged battery during folding.

[37–44]. To quantitatively investigate the vanadium dissolution behavior, inductively coupled plasma mass spectrometry (ICP-MS) was employed in this study. Specifically, IO–NVO and pristine NVO samples were immersed in 2.0 mol/L $Zn(CF_3SO_3)_2$ electrolyte for 10 days. The results show that the vanadium solubility of IO–NVO (0.252 mg/L) is significantly lower than that of NVO (0.333 mg/L). This finding confirms that dual-guest co-intercalation can effectively enhance the exposure of active sites and inhibit vanadium dissolution thus constructing a stable framework and providing a key prerequisite for the efficient storage of large amounts of Zn^{2+} (Fig. S13 in Supporting information).

To comprehensively evaluate the electrochemical performance of the Zn||IO–NVO battery, a flexible aqueous zinc ion battery was assembled in this study. IO–NVO as the cathode material, metallic zinc as the anode material, and 2.0 mol/L $Zn(CF_3SO_3)_2$ as the electrolyte. As an electrode separator, a glass fiber membrane was used on the flexible battery assembly, which was encapsulated in an aluminum plastic film (Fig. 3f). An electrochemical characterization revealed a specific capacity of 326.2 mAh/g at 0.8 A/g (Fig. 3g and Fig. S14a in Supporting information). After 100 cycles, the device retained 76.60 % of its capacity, conditions. Mechanical tests at bending angles of 0°, 45°, 90°, and 180° confirmed its structural integrity under deformation. These results indicate that the battery remains electrochemically stable even under extreme battery remains electrochemically stable even under extreme bending conditions, proving its excellent resistance to mechanical damage. The flexible battery based on IO–NVO also exhibited outstanding stability and flexibility (Fig. 3h and Fig. S14b in Supporting information). It demonstrated excellent stability and flexibility by continuously displaying the pattern "JJU" at different bending angles of 0°, 45°, 90°, and 180° using two flexible battery cells connected in series. To explore its application potential under high mass loading, relevant tests were conducted on IO–NVO at a high mass loading of 4.25 mg/cm^2. In terms of cycling performance, the material maintained a capacity retention rate of 92.00 % with a specific capacity of 130.5 mAh/g after 4000 cycles at 6.0 A/g (Fig. S14c in Supporting information). The battery also demonstrated excellent rate capabilities at different current densities, delivering an excellent specific capacity of 327.1 mAh/g with 0.2 A/g current density, and maintaining that capacity when the current density returned to 0.5 A/g (Fig. S14d in Supporting information). The cathode achieved an energy density of 632.02 Wh/kg at 0.2 A/g, which is higher than that of most vanadium-based cathodes reported to date (Fig. S14e in Supporting information). In addition to providing valuable insights for the development of flexible electronics and wearable energy systems, these advances also provide a solid foundation for their practical application.

An electrochemical kinetic analysis was used to determine the kinetic behavior of the IO–NVO cathode. CV tests were conducted between 0.2 mV/s and 1.0 mV/s within a voltage window of 0.2–1.6 V (Fig. 4a). There are multiple redox peaks observed on the CV curve due to vanadium ions in distinct oxidation states, suggesting a multi-step Zn^{2+} intercalation process. Although the overall shape of the CV curve remains largely unchanged, the anodic peaks exhibit a positive shift and the cathodic peaks exhibit a negative shift with increasing scan rate. Applying the power-law relationship ($i = av^b$) [45,46], the b-values for two representative redox peak pairs were determined by linearly fitting log(i) *vs.* log(v). Generally, a b-value of 0.5 indicates a diffusion-controlled process, whereas a value of 1.0 indicates a capacitive-dominated reaction, with experimental values typically lying between these limits [47]. The calculated b-values for the two redox peak pairs are 0.90/0.84 and 0.99/0.88 respectively, demonstrating that charge storage at the IO–NVO electrode is primarily governed by pseudocapacitive processes (Fig. 4b). Consistent with this finding, the capacitive contribution ratio increases from 87.97 % to 97.26 % with an increasing scan rate (Fig. 4c). Underscoring the enhanced role of surface-controlled mechanisms at higher rates. In the case of an

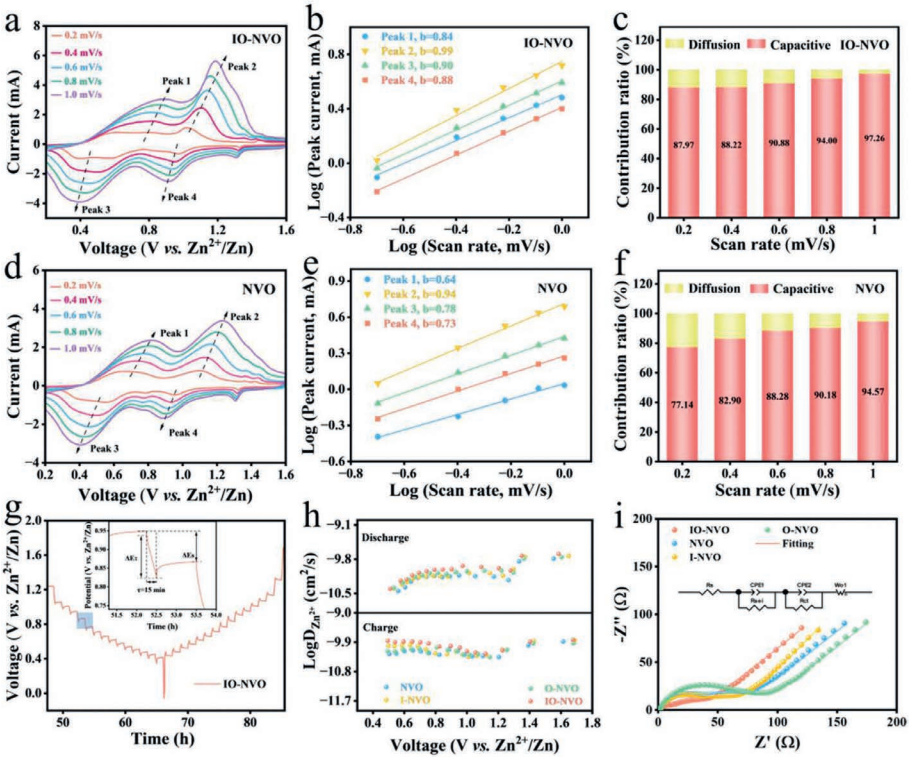


Fig. 4. Electrochemical kinetics and ion diffusion behavior of the IO–NVO and NVO electrode. (a, d) Cyclic voltammetry curves of IO–NVO and NVO. (b, e) Current-scan rate relationships plotted as log(*i*) *vs.* log(*v*) for the four redox peaks of IO–NVO and NVO. (c, f) Capacitive and diffusion-controlled contribution ratios at various scan rates of IO–NVO and NVO. (g) Comparison chart of GITT for IO–NVO. (h) Galvanostatic intermittent titration technique (GITT) potential profiles and corresponding $D_{Zn^{2+}}$ values. (i) Nyquist plots collected after cycling.

IO–NVO at 1.0 mV/s, the capacitive contribution reached 97.26%, which is significantly more than that of NVO (94.57%), I-NVO, and O–NVO (Figs. 4d-f, Figs. S15 and S16 in Supporting information). In addition, galvanostatic intermittent titration (GITT) was used to investigate the kinetics of ion diffusion. A comparison of the Zn^{2+} diffusion coefficients ($D_{Zn^{2+}}$) reveals that IO–NVO exhibits significantly higher values ($10^{-10.40}$–$10^{-9.69}$ cm^2/s) compared to I-NVO ($10^{-10.40}$–$10^{-9.73}$ cm^2/s), O–NVO ($10^{-10.41}$–$10^{-9.75}$ cm^2/s), and NVO ($10^{-10.45}$–$10^{-9.79}$ cm^2/s) (Figs. 4g and h, Fig. S17 in Supporting information), demonstrating its superior ionic diffusion properties. This demonstrates the advantage of Al^{3+} and $BTMA^+$ co-intercalation in enhancing Zn^{2+} diffusion kinetics. Electrochemical impedance spectroscopy (EIS) revealed a significantly lower initial charge transfer resistance (R_{ct}) for IO–NVO (105 Ω) than NVO (338 Ω) (Fig. S18 in Supporting information). After 5 cycles, electrode activation reduced the R_{ct} for all samples, with IO–NVO maintaining a significantly lower impedance than the other three materials (Fig. 4i). Nyquist plots of the electrochemical impedance spectroscopy tests do not show the characteristics of standard single semicircles but clearly show double semicircles. The electrochemical process with double time constants includes the formation of SEI films and charge transfer at the electrode interface. To accurately fit the impedance response, an equivalent circuit consisting of solution resistance and two constant phase elements was selected. It was also used to analyze the interfacial dynamic behavior. The first time constant represents CPE1 and SEI film resistance in the high frequency region, the second one represents CPE2 and charge transfer resistance, and W represents diffusion behavior in the low frequency region. The consistency of the curves before and after fitting indicates that the equivalent circuit is suitable.

To elucidate the Zn^{2+} storage mechanism during IO–NVO electrochemical processes, we conducted *ex-situ* XRD/XPS characterizations on electrodes harvested at selected states (Fig. 5a). *Ex-situ* spectroscopic characterizations of the IO–NVO cathode enabled a systematic investigation of its structural evolution and charge storage mechanism. In the *ex-situ* XRD patterns (Fig. 5b), the (001) peak of IO–NVO shifts to a lower angle during the initial discharge process (State A → B), directly indicating that the intercalation of Zn^{2+} into the interlayers of IO–NVO leads to an expansion of the interlayer spacing. After charging (State B → D), the (001) peak reverts to its original position, demonstrating the material's good structural reversibility. During the subsequent discharge stage (State D → F), the (001) peak shifts to a lower angle again, accompanied by the emergence of new characteristic peaks at approximately 17.3°, 25.8°, and 30.1°. The emergence of these new peaks is attributed to the formation of a stable heterophase, $Zn_3(OH)_2V_2O_7{\cdot}2H_2O$ [48,49], after the first cycle. Heterophase exhibits excellent reversibility, acting as a buffer layer to stabilize the IO–NVO framework during cycling, rather than indicating irreversible structural degradation [50]. To gain a deeper understanding of the electrochemical behavior, we conducted *in-situ* Raman spectroscopy analysis (Fig. 5c). The characteristic peaks at 168, 272, 404, and 412 cm^{-1} gradually weaken with the intercalation of Zn^{2+}. Zn 2p peaks increase significantly in intensity when fully discharged (Fig. 5d) indicating that many Zn^{2+} ions are intercalated into the layered structure during discharge. After charging to 1.6 V, residual Zn^{2+} signals are still detectable, which may stem from the surface heterogeneous phase $Zn_3(OH)_2V_2O_7{\cdot}2H_2O$. The weak zinc signal observed is attributed to zinc adsorption by the pristine IO–NVO, with all test samples acquired *via ex-situ* characterization. The *ex-situ* O 1s XPS spectrum (Fig. 5e) reveals a weak H_2O peak at 532.78 eV, supporting the hypothesis that the expanded interlayer spacing of the as-prepared NVO arises from the presence of crystalline water. Upon full discharge, the intensity of this peak increases remarkably, and after recharging to 1.6 V, it nearly reverts to the pristine state. This reversible variation indi-

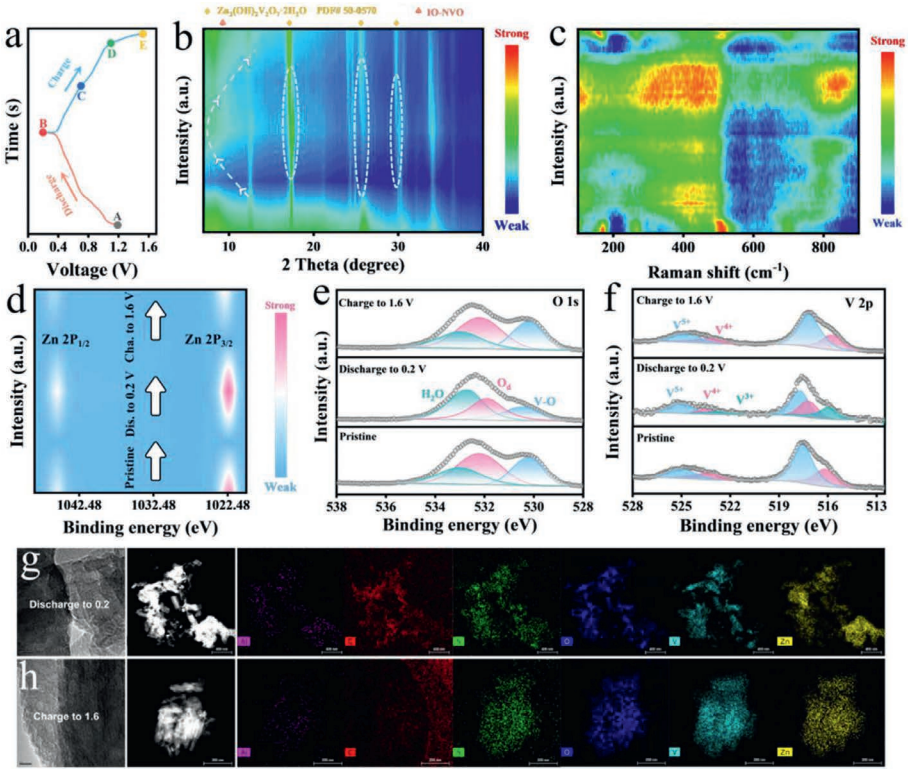


Fig. 5. Investigation of the energy storage mechanism in IO–NVO. (a) GCD curve at 0.1 A/g and corresponding (b) *ex-situ* XRD patterns for the first cycle. (c) *In-situ* Raman spectra at various cycling stages. (d-f) *Ex-situ* XPS spectra of Zn 2p, O 1s, and V 2p acquired at selected potentials. (g, h) HRTEM images, TEM and elemental mapping images (under the fully discharged/charged states).

cates the co-intercalation of H_2O (accompanied by H^+) and Zn^{2+}, along with the formation of $Zn_3(OH)_2V_2O_7{\cdot}2H_2O$, and these observations are consistent with the *ex-situ* XRD results.These results confirm that both H^+ and Zn^{2+} participate in the electrochemical reaction. In addition, it has been shown that Zn^{2+} intercalation led to a partial reduction of V^{5+} to V^{4+} and V^{3+}, thus altering its electronic distribution (Fig. 5f). Upon charging to 1.6 V, the V 2p signal nearly reverts to its initial state, confirming the reversibility of the vanadium redox reaction, a finding consistent with the O 1s spectral evolution. We conducted high-resolution transmission electron microscopy, energy-dispersive X-ray spectroscopy mapping, and Fourier transform infrared spectroscopy analyses of the IO–NVO cathode sample subjected to 50 consecutive charge-discharge cycles at 2.0 A/g to verify the changes in the layered structure of IO–NVO after long-term cycling. The elemental distribution results of the fully discharged and charged IO–NVO clearly demonstrate that carbon, nitrogen, aluminum and zinc are uniformly distributed across the entire cathode surface without local aggregation or depletion, indicating the highly reversible process of Zn^{2+} insertion and extraction (Figs. 5g and h). This confirms that Al^{3+} and $BTMA^+$ ions remain intercalated within the layers after long-term. In addition, further support is obtained from FTIR spectrum analysis (Fig. S19 in Supporting information), where the characteristic peaks of $BTMA^+$ (pH, C–N bond) appear at 1036.66 and 1261.33 cm^{-1}, while the peak at 1388.33 cm^{-1} provides strong evidence for the presence of Al. These observations directly confirm that Al^{3+} and $BTMA^+$ are firmly retained in the interlayers of NVO during repeated electrochemical cycling and that IO–NVO exhibits high reversibility, which is essential for maintaining the structural integrity and long-term electrochemical performance of the IO–NVO cathode. Based on these findings, the reaction mechanism is proposed as follows: Zn^{2+} ions intercalate into the IO–NVO interlayers, forming the hetero-phase $Zn_3(OH)_2V_2O_7{\cdot}2H_2O$ after the first full discharge. Charging to 1.6 V deintercalates Zn^{2+}, leaving residual Zn^{2+} and a small amount of $Zn_3(OH)_2V_2O_7{\cdot}2H_2O$, indicating the hetero-phase contributes to Zn^{2+} storage. The IO–NVO cathode exhibits distinct morphological evolution across different electrochemical states (Fig. S20 in Supporting information). The pristine cathode surface is smooth, while upon full discharge it becomes covered with a by-product identified as $Zn_3(OH)_2V_2O_7{\cdot}2H_2O$. These secondary phases disappear after full charging, restoring the cathode to its initial morphology. Reversible microstructural evolution is consistent with the *ex-situ* XRD/XPS results, confirming the highly reversible and facile intercalation/deintercalation of Zn^{2+} within the V-O interlayer.

In summary, this study employs a facile one-step solvothermal method to modify the NVO cathode *via* a $BTMA^+/Al^{3+}$ dual-guest synergistic intercalation strategy, which enables molecular pillaring and electronic modulation of ammonium vanadate while synergistically expanding the interlayer spacing to 10.9 Å. This modification further enlarges the specific surface area to expose more active sites; moreover, DFT calculations confirm that the modified material exhibits enhanced electrical conductivity and elevated adsorption energy toward Zn^{2+}, thereby facilitating accelerated ion diffusion kinetics. Benefiting from the synergistic effects of molecular pillaring and electronic modulation, the IO–NVO material delivers outstanding electrochemical performance, including a high specific capacity of 432.8 mAh/g at 1.0 A/g, a retained capacity of 320.1 mAh/g at 6.0 A/g, and 92.07 % capacity retention after 2000 cycles. The H^+/Zn^{2+} co-intercalation/deintercalation mechanism was elucidated through *in-situ* Raman and *ex-situ* XRD/XPS analyses, confirming structural stability and enhanced ion transport enabled by the dual-guest modification strategy. Therefore, the Zn||IO–NVO battery demonstrates excellent capacity, excellent rate performance, high load capability, and long-term cycling stability, fully demonstrating the potential of inorganic-

organic co-intercalation technology in designing high-performance ammonium vanadate cathode materials, providing crucial support for the application of advanced AZIBs.

CRediT authorship contribution statement

Chengjun Wu: Writing – original draft, Formal analysis, Data curation. **Yajiang Wang:** Validation, Data curation. **Xiaoduo Jiang:** Investigation. **Huixiong Jiang:** Visualization. **Jin-Hang Liu:** Software. **Ping Yan:** Resources. **Hai-Yan Hu:** Methodology. **Yao Xiao:** Writing – review & editing, Supervision, Project administration. **Xiudong Chen:** Writing – review & editing, Funding acquisition, Conceptualization.

Declaration of competing interest

The authors declare that they have no known competing financial interests or personal relationships that could have appeared to influence the work reported in this paper.

Acknowledgments

This work was supported by the National Natural Science Foundation of China (No. 22163003), Jiangxi Province Double Thousand Plan (No. jxsq2023201091), the Jiangxi Provincial Natural Science Foundation (Nos. 20262BAC220059, 20232BAB203024), Science and Technology Project of Jiangxi Provincial Department of Education (Nos. GJJ2401837, GJJ2501824), Jiujiang Science and Technology Project (Nos. 2025_00174, 2025_00670).

Supplementary materials

Supplementary material associated with this article can be found, in the online version, at doi:10.1016/j.cclet.2026.112787.

References

[1] M. Han, Y. Ding, J. Lou, et al., Energy Environ. Sci. (2026) 1754–5692.
[2] X. Chen, X. Hu, Y. Chen, et al., J. Mater. Chem. A 10 (2022) 22194.
[3] C. Zhou, L. Shan, Z. Xing, et al., Adv. Mater. 38 (2026) e16045.
[4] X. Fu, Y. Pan, Z. Chen, et al., Energy Environ. Sci. 4 (2026) 1170–1179.
[5] X. Chen, H. Jiang, J. Liu, et al., Adv. Funct. Mater. 35 (2025) 2421697.
[6] Z. Xing, P. Ye, X. Shi, et al., Angew. Chem. Int. Ed. 64 (2025) e202516974.
[7] D. Qi, H. Jiang, X. Chen, et al., ACS Nano 19 (2025) 24592.
[8] Y. Wang, Y. Fan, X. Chen, et al., InfoMat 7 (2025) e70055.
[9] J. Bai, S. Hu, L. Feng, et al., Chin. Chem. Lett. 35 (2024) 109326.
[10] Y. Xin, M. Zhu, H. Zhang, X. Wang, Nano-Micro Lett. 18 (2025) 2150–5551.
[11] Y. Li, C. Zhao, Y. Xu, et al., Nano Res. Energy 4 (2025) e9120173.
[12] D. Chen, J. Fu, Y. Ming, et al., Nano-Micro Lett. 18 (2025) 48.
[13] Z. Xing, P. Ye, X. Shi, et al., Angew. Chem. Int. Ed. 64 (2025) e202516974.
[14] C. Zhao, Y. Liu, S. Li, X. Wu, J. Liu, Chin. Chem. Lett. 36 (2025) 110185.
[15] X. Chen, J. Liu, H. Jiang, et al., Energy Storage Mater. 65 (2024) 103168.
[16] J. Kim, S. Lee, C. Park, et al., Adv. Funct. Mater. 31 (2021) 2100005.
[17] K. Wang, R. Yuan, M. Li, et al., Chem. Eng. J. 471 (2023) 144655.
[18] Q. Li, X. Rui, D. Chen, et al., Nano-Micro Lett. 12 (2020) 67.
[19] H. Li, J. Yang, J. Cheng, T. He, B. Wang, Nano Energy 68 (2020) 104369.
[20] Q. Zong, Q. Wang, C. Liu, ACS Nano 16 (2022) 4588–4598.
[21] Y. Chen, X. Li, X. Zhao, X. Cheng, J. Liu, Appl. Surf. Sci. 509 (2020) 145079.
[22] B. Dong, N. Shen, C. Cao, et al., CrystEngComm 18 (2016) 558–565.
[23] X. Jia, C. Liu, Z. Wang, D. Huang, G. Cao, Nano-Micro Lett. 16 (2024) 2150–5551.
[24] H. Gökce, S. Bahçeli, Z. Für, Naturforschung A 64 (2009) 127–131.
[25] Y. Xu, H. Dong, M. Zhou, et al., Small Methods 3 (2018) 1800349.
[26] D. Fang, Y. Cao, R. Liu, et al., Appl. Surf. Sci. 360 (2016) 658.
[27] S. Kong, Y. Li, X. Zhang, et al., Small 19 (2023) 2304462.
[28] K. Guo, Z. Song, Y. Lv, L. Gan, M. Liu, Adv. Funct. Mater. 35 (2025) 2506036.
[29] L. Xing, C. Zhang, M. Li, et al., Energy Storage Mater. 52 (2022) 291–298.
[30] X. Wang, Y. Wang, A. Naveed, et al., Adv. Funct. Mater. 33 (2023) 2036205.
[31] Y. Zeng, Z. Lai, Y. Han, et al., Adv. Mater. 30 (2018) 1802396.
[32] J. Wang, Z. Zhang, X. Zhang, et al., Nano Energy 39 (2017) 647–653.
[33] S. Kong, Y. Li, X. Zhang, et al., Small 19 (2023) 2304462.
[34] W. Shi, B. Yin, Y. Yang, et al., ACS Nano 15 (2021) 1273–1281.
[35] Q. Zong, W. Du, C. Liu, et al., Nano-Micro Lett. 13 (2021) 116.
[36] W. Kang, B. Zhang, Z. Wang, et al., J. Energy Chem. 94 (2024) 608.
[37] D. He, Y. Peng, Y. Ding, et al., J. Power. Sources 484 (2021) 229284.
[38] Q. Wang, J. Wu, M. Wang, et al., Adv. Sci. 11 (2024) 2307872.
[39] G. Yang, T. Wei, C. Wang, ACS Appl. Mater. Interfaces 10 (2018) 35079.
[40] P. Hu, M. Yan, T. Zhu, et al., ACS Appl. Mater. Interfaces 9 (2017) 42717.
[41] W. Nie, P. Sun, S. Xu, et al., Colloid. Surf. A 674 (2023) 131891.
[42] K. Wang, H. Li, G. Guo, et al., ACS Energy Lett. 8 (2023) 1671.
[43] J. Zhang, W. Li, J. Wang, et al., Angew. Chem. Int. Ed. 62 (2023) 202215654.
[44] W. He, C. Meng, Z. Ai, et al., Chem. Eng. J. 454 (2023) 140260.
[45] N. Zhang, Y. Dong, M. Jia, et al., ACS Energy Lett. 3 (2018) 1366–1372.
[46] D. Chao, C. Zhu, M. Song, et al., Adv. Mater. 30 (2018) 1803181.
[47] D. Wu, W. Zhang, Y. Feng, J. Ma, J. Mater. Chem. A 8 (2020) 2618.
[48] J. Sun, Y. Liu, H. Jiang, et al., J. Colloid Interf. Sci. 602 (2021) 14.
[49] Z. Feng, Y. Zhang, J. Sun, et al., Chem. Eng. J. 433 (2022) 133795.
[50] Y. Yang, Y. Tang, S. Liang, et al., Nano Energy 61 (2019) 617.